metals

Article

Physical and Mechanical Properties of Ti-Zr-Nb Alloys for Medical Use

Konstantin V. Sergienko [1,*], Sergei V. Konushkin [1], Mikhail A. Kaplan [1], Artem D. Gorbenko [1], Yucheng Guo [2], Elena O. Nasakina [1], Maria A. Sudarchikova [1], Tatiana M. Sevostyanova [3,4], Yaroslava A. Morozova [1], Lyudmila A. Shatova [5], Sofia A. Mikhlik [1], Mikhail A. Sevostyanov [1] and Alexey G. Kolmakov [1]

[1] A.A. Baikov Institute of Metallurgy and Materials Science, Russian Academy of Sciences (IMET RAS), 119334 Moscow, Russia; venev.55@mail.ru (S.V.K.); mishakaplan@yandex.ru (M.A.K.); artemgorbenk@yandex.ru (A.D.G.); nacakina@mail.ru (E.O.N.); mariahsudar@yandex.ru (M.A.S.); yasya12987@gmail.com (Y.A.M.); beliyfecity@yandex.ru (S.A.M.); cmakp@mail.ru (M.A.S.); akolmakov@imet.ac.ru (A.G.K.)
[2] Department of Materials Science, Bauman Moscow State Technical University (BMSTU), 105005 Moscow, Russia; guobmstu@outlook.com
[3] National Medical and Surgical Center Named after N.I. Pirogov of the Ministry of Health of the Russian Federation, 117513 Moscow, Russia; tata_sev1048@mail.ru
[4] Moscow Regional Research and Clinical Institute ("MONIKI"), 129110 Moscow, Russia
[5] Faculty of Radio Engineering and Electronics, Voronezh State Technical University, 394026 Voronezh, Russia; lashatova1@mail.ru
* Correspondence: shulf@yandex.ru; Tel.: +7-9581998137

Abstract: The work described in this article is aimed at investigating the properties of a group of Ti-Zr-Nb alloys. In modern orthopedics and traumatology, the use of materials for bone implants with a minimum modulus of elasticity is becoming increasingly important. This is due to a number of advantages that allow for better integration of the implants with the bone tissue, including the reduction in the detrimental effect of the load-shielding effect, a better load distribution, and stress distribution, which allows for increasing the life of the implant. It is known that the lowest modulus of elasticity in titanium alloys at normal temperature is achieved by the phase composition consisting of metastable β-phase. It is possible to achieve the desired structure by a combination of alloy composition selection and heat treatment. Quenching of titanium alloys allows for the high-temperature β-phase to be fixed. This paper provides justification of the choice of compositions of the studied alloys by calculation methods. The structure of alloys after melting in a vacuum electric arc furnace in an argon environment was studied. The ingots obtained had a dendritic structure. Homogenizing annealing in a vacuum furnace at 1000 °C for 4 h was used to equalize the composition. The structure of the alloyed sheets after hot rolling and hot rolling and quenching was investigated. The microstructure of the plates in both variants had uniform grains of polyhedral shape. X-ray phase analysis of the plates showed that the content of metastable β-phase was 100% before and after quenching. Microhardness testing of the plates showed no significant effect of quenching. The result of the mechanical properties study showed an increase in the plasticity of the material after quenching, with the tensile plots of the samples after quenching reflecting the area where the reverse phase transition of β'<-> α" occurs. Mechanical studies by cyclic loading showed the presence of a superelasticity effect. The Young's modulus study gave a result of 51 GPa for one of the compositions studied. The combination of properties of the materials under investigation has the potential for promising use as a basis for bone implants.

Keywords: titanium alloys; zirconium alloys; Young's modulus; mechanical properties; implants; medical materials

check for updates

Citation: Sergienko, K.V.; Konushkin, S.V.; Kaplan, M.A.; Gorbenko, A.D.; Guo, Y.; Nasakina, E.O.; Sudarchikova, M.A.; Sevostyanova, T.M.; Morozova, Y.A.; Shatova, L.A.; et al. Physical and Mechanical Properties of Ti-Zr-Nb Alloys for Medical Use. *Metals* **2024**, *14*, 1311. https://doi.org/10.3390/met14111311

Academic Editor: Jürgen Eckert

Received: 16 October 2024
Revised: 9 November 2024
Accepted: 15 November 2024
Published: 20 November 2024

Copyright: © 2024 by the authors. Licensee MDPI, Basel, Switzerland. This article is an open access article distributed under the terms and conditions of the Creative Commons Attribution (CC BY) license (https://creativecommons.org/licenses/by/4.0/).

1. Introduction

The continuous striving of mankind to improve quality of life demands new materials for all fields of science and technology, especially so for medicine, for implants in particular. Previously used cobalt alloys and stainless steel, despite their good strength characteristics and corrosion resistance, contain elements toxic to the human body and have an elastic modulus many times higher than the elastic modulus of human bone tissue [1–5]. So, the non-magnetic alloy ASTM F75-2007 [6] used earlier as a material for bone implants has tensile strength σv up to 860 MPa, yield strength $\sigma_{0.2}$ ~ 759 MPa, and Young's modulus E ~ 220 GPa, and the stainless austenitic steel AISI 316L replacing it has σv ~ 485 MPa, $\sigma_{0.2}$ ~ 170 MPa, and E ~ 210 GPa.

Mechanical Compatibility with Bone Tissue: One of the most important aspects in the development of bone implant materials is their mechanical compatibility with bone. For bone implants, both the stiffness (Young's modulus) and the deformability of the material must be considered. Human bone has a certain modulus of elasticity that is much lower than that of traditional metallic materials such as titanium alloy. Young's modulus E is a measure of a material's stiffness that describes its ability to resist tension or compression. The implant material should have the E value as close as possible to its values for bone (up to 30 GPa) [7,8]. In this case, such a material will provide better mechanical biocompatibility between the implant and the bone in which it is fixed, thus avoiding excessive local overstretching of bones and joints and uneven load distribution. If the implant is too stiff compared to the surrounding bone, it can absorb most of the mechanical load, resulting in weakening and atrophy of the bone in contact with the implant. This phenomenon is called stress shielding. In such cases, the bone is not subjected to normal physiological stresses and its structure may weaken [9–12]. Resulting in the need for repeated surgical intervention with implant replacement [13].

In recent years, α + β and β titanium (BCC (body-centered cubic) lattice) alloys have become a key focus of research as a material for the next generation of joint endoprostheses due to their potentially promising set of properties. The most commonly used titanium alloys to date are α titanium (CP Grade 4) and α + β titanium alloy (Ti-6Al-4V, CP Grade 5), which have, respectively, σv ~ 550 MPa and ~ 925 MPa, σ0.2 ~ 483 MPa and ~ 900 MPa, and E ~ 102 and ~ 113 GPa. These are excessive values of elasticity in relation to bone tissue, which has E ~ 20–35 GPa [7,8]. In addition, alloying titanium with aluminum and vanadium creates long-term risks for the patient's health, since the neurotoxic effect of excessive amounts of aluminum is known, contributing to the development of Parkinson's and Alzheimer's disease when aluminum accumulates in the brain [14,15]. Additionally, the effects of excess aluminum on male sexual function have been noted [16]. Systematic exposure to vanadium can lead to diarrhea, nausea, loss of appetite and weight loss, and impaired male fertility [17–19]. At the same time, modern studies of biocompatibility of niobium, zirconium, alloys with them, as well as their oxides, do not reveal any risks in long-term use as materials for implantation in the human body [20–24].

Superelastic materials have a lower modulus of elasticity and can distribute the load better, minimizing the risk of stress shielding effects. This allows for the bone to continue to function normally, helping to preserve and strengthen the bone around the implant. Superelasticity effect helps bone implant materials withstand cyclic loading (e.g., walking, running, lifting weights) without fatigue cracking. Superelastic materials can compensate for small changes in shape under load and return to their original state without permanent deformation, preventing the development of microcracks and increasing the life of the implant.

In this context, it is necessary to develop titanium alloys with high mechanical properties, low E value, and safe chemical elements. In particular, it is known that titanium alloys with metastable β-phase (β', BCC (body-centered cubic) lattice), have the lowest E value, which can be obtained by selecting the alloy composition and heat treatment from the (α + β) phase, while avoiding the release of brittle and hard ω-phase. Ti β-type alloys were confirmed to have the lowest Young's modulus. It should be noted that the majority of

Ti β-type alloys with low Young's modulus contain Nb as a β-stabilizing alloying element due to its moderate β-phase-stabilizing ability and biocompatibility [25–32].

In addition to the literature data, a computational method for estimating the initial phase composition by the molybdenum equivalent method [27] was used to evaluate the stability of the β-phase and optimize the alloy composition, as well as the experience of a previous study [33–35].

One of the most promising systems of such alloys is the Ti-Zr-Nb system. In recent years, there has been a growing interest in Ti-Zr-Nb and Ti-Nb-Zr alloys for medical applications. These materials have attracted attention due to their favorable combination of properties that make them promising for use as implantable devices such as endoprostheses. The inclusion of zirconium (Zr) and niobium (Nb) in the titanium alloy provides both the necessary durability of implants and maintains their low density and excellent corrosion resistance, low modulus of elasticity, and, in some combinations of elements, superelasticity, which is critical to ensure long-term functionality in the body environment [36–40].

The purpose of this study is to develop and comprehensively evaluate a titanium alloy containing zirconium and niobium for use as a material for bone implants. In the course of this work, the task was set to comprehensively analyze the influence of composition and thermomechanical processing on the structural and phase characteristics, as well as on the mechanical, cyclic, and superelastic properties of the alloy. Particular attention was paid to the study of the Young's modulus as a key parameter that determines the mechanical compatibility of the material with human bone, which is important for improving durability and functional efficiency in implants. In this work, the physical and mechanical properties of Ti-(36-40)Zr-9Nb alloys (at.%) were investigated.

2. Materials and Research Methods

2.1. Selection of the Object of Research

Three alloys were investigated (at.%): Ti-36Zr-9Nb, Ti-38Zr-9Nb, and Ti-40Zr-9Nb. Titanium produced by company VSMPO-AVISMA Corporation (Russia) was used, Zirconium and Niobium produced by company Chepetskiy Mechanical Plant (Russia) were used. The Mo equivalent is an empirical parameter representing the contribution of the alloying elements to the stability of the β-phase relative to Mo [32].

To perform the calculation, it is necessary to convert atomic percentages into mass percentages:

Let us take the example of the Ti-36Zr-9Nb alloy (Table 1):

Table 1. Conversion of atomic percentage to mass percentage.

Chemical Element	Atomic Mass (a.e.m.)	Atomic Percentage (%)	Atomic Mass * Atomic Percent =	Mass Percentage (%)
Ti	47.87	55	2632.85	38.99
Nb	92.91	9	836.16	12.38
Zr	91.22	36	3283.92	48.63

Taking into account the mass percentages and literature data on the contribution of the alloying elements, we calculate

[Mo] eq = (x(i) × C(Mo))/(C(i)), where C(i) and C(Mo) are the second critical concentrations of the alloying element and molybdenum, respectively [32].

When estimating the molybdenum equivalent of a complex alloy, the effect of different β-stabilizers is considered additive and the influence of α-stabilizers and neutral hardeners is neglected. Thus,

[Mo] eq%Nb/3,6 + %Zr/14.

The effect of Nb on β-phase stability is 1/3.6, i.e., niobium is 3.6 times weaker in stabilizing the beta-phase and zirconium is 14 times weaker than molybdenum.

Calculation of the molybdenum equivalent for 1-Ti-9Nb-36Zr, 2-Ti-9Nb-38Zr, and 3-Ti-9Nb-40Zr:

[Mo] eq = %Nb/3.6 + %Zr/14 = 12.38/3.6 + 48.63/14 = 6.91
[Mo] eq = b/3.6 + %Zr/14 = 12.22/3.6 + 50.68/14 = 7.01
[Mo] eq = %Nb/3.6 + %Zr/14 = 12.02/3.6 + 52.87/14 = 7.11

It can be concluded that all the alloys studied have an α+β phase based on the data obtained and the information in Table 2 in the annealed state; therefore, by means of thermomechanical treatment, namely, plastic deformation and quenching, alloys with unstable β-phase, low Young's modulus, and superelasticity effect can be obtained from them.

Table 2. Value of molybdenum equivalent as a function of alloy phase composition (Adapted from Ref. [32]).

Alloy Grade	[Mo] Equivalent
(α + β)-alloys	3.3–10
Pseudo β-alloys	11.0–16.3
β-alloys	16.9

2.2. Production and Processing of Research Samples

The alloy samples were melted in a copper water-cooled crystallizer in an argon arc furnace with a non-expendable tungsten electrode L200DI (Leybold-Heraeus, Hanau, Germany) at an argon pressure of 40×10^3 Pa. The following were used as charge materials: titanium (Ti-1 grade), zirconium (Zr-1 grade), and niobium (Hb-1 grade). The materials were placed in a copper water-cooled tray of a vacuum electric arc furnace as follows: titanium was placed at the bottom of the crystallizer wells, then zirconium, and niobium on top. The order of arrangement of initial metals corresponded to the melting temperature of each material, and melting was carried out by arc directed from top to bottom. Additionally, zirconium was placed in a separate tray to act as a getter. The furnace was vacuumized to a residual pressure of 1.33 Pa, filled with inert argon gas of high purity. At first, the zirconium getter is melted after induction into the inert gas chamber to remove possible oxygen impurities in the gas. Next, melting of the starting materials is performed until the formation of single ingots. Remelting was carried out 7 times with ingots turning over for better mixing of initial components.

The obtained ingots have a dendritic structure. Homogenizing annealing in a vacuum resistance furnace ESKVE-1.7.2.5/21 ShM13 (NITTIN, Moscow, Russia) at 1000 °C for 4 h was used to homogenize the structure and remove stresses. To protect against oxidation, annealing was performed in a vacuum environment at 27×10^{-4} Pa.

Primary deformation of ~18 mm thick castings was carried out by warm rolling at preheating to a temperature of 600 °C on a double-roller mill, DUO-300 (AO Istok ML, Fryazino, Moscow Oblast, Russia), with partial absolute compressions per pass: 1.5 mm down to billet thickness of 4.0 mm (heating every 2 passes, total 10 passes), then 1.0 mm down to billet thickness of 2.0 mm (heating every pass, total 2 passes), and a further 0.5 mm down to final billet thickness—1 mm (heating before the first pass at thickness of 2 mm, total 2 passes). The billets were heated before deformation in a muffle furnace KYLS 20.18.40/10 (Hans Beimler, Leipzig, Germany) to a temperature of 600 °C for 20 min before the first rolling and for 5 min during intermediate annealing. The plates were cold-rolled from a thickness of 1.5 mm. The effect of heat treatment on the structure and mechanical properties of Ti-(36-40)Zr-9Nb alloys was investigated on plate samples with a final thickness of 1 mm. Hardening of the samples was carried out after heating for 5 min at 600 °C in room temperature water. During rolling and quenching, a thin oxide layer formed on the surface of the samples. This layer was removed by mechanical grinding.

Preparation of samples for metallographic study was carried out by sequential grinding on a Buehler Phoenix 4000 machine (Lake Bluff, IL, USA). The microstructure was revealed and analyzed by etching in a weak solution of hydrofluoric and nitric acids with distilled water in the ratio of 10% HF: 10% HNO_3: 80% H_2O for 20–30 s. After, the microstructure was rinsed with distilled water, and residual water was removed by air flow. Light

microscopy was carried out on Altami MET 5C (Altami, Saint Petersburg, Russia) microscope using a high-resolution video camera built into the device and Altami Studio 3.5 software.

2.3. Methods of Research

The direct measurement method was used to estimate the grain size: This method uses scale bars on the image and image processing software. A virtual ruler on the image is used to measure the average diameter of the grains. Considering that the shape of grains is different, several straight line measurements (width and length) were taken for elliptical or polyhedral grains and the average value is calculated.

X-ray diffractograms were obtained on an ARL X'TRA instrument (Thermo Fisher Scientific (Ecublens) sarl, Ecublens, Switzerland), in CuKα-radiation in parallel beam geometry. The instrument was calibrated to the NIST SRM-1976a [41] standard pattern, and the error in the position of the reflexes did not exceed 0.01° 2q. The crystal lattice parameter was refined by extrapolation to q = 90° by the Nelson–Riley method using Origin-2017 software. The quantitative content of crystalline phases was estimated by the method of corundum numbers. Before study, the surface of the samples was cleaned with emery paper (P4000) with subsequent washing in ethyl alcohol and distilled water.

To study microhardness, the Vickers method was used at a load of 200 g and a dwell time of 15 s on microhardness tester 401/402-MVD, manufactured by Instron Wolpert Wilson Instruments (Norwood, MA, USA). The microhardness of plates after rolling and quenching at 600 °C was investigated.

Static mechanical tests were performed on a universal testing machine INSTRON 3382 (Instron, Norwood, MA, USA) with a tensile speed of 1 mm/min using flat specimens of 28 × 6 × 1 mm and a working part size of 15 × 3 × 1 mm. The number of specimens for each alloy type and treatment type was 9 pieces. Processing of test results in determining the characteristics of mechanical properties was carried out in accordance with GOST 1497-84 using INSTRON Bluehill 2.0 software. The following characteristics were determined: conditional yield strength $\sigma_{0.2}$, tensile strength σv, and relative elongation δ. Determination of E values was carried out in static tensile testing of the specimens using an extensometer.

Cyclic tests to determine the hysteresis behavior of the material were performed on an INSTRON 3382 universal testing machine. For each specimen, 10 cycles were performed; in the first part of the cycle, the specimen was stretched at a rate of 1 mm/min until the working area was elongated by 8%, and in the second part of the cycle, the specimen was compressed at a rate of 1 mm/min to the original size. The best hysteresis behavior can be used to evaluate the superplasticity effect of the alloys studied. Strain measurement was performed with an additional probe mounted directly on the specimen with two clamps along the edge of the specimen work area, so that the tensile value of the specimen work area was more accurate and did not include the strain of the gripping parts of the specimen, which occurs when using tensile values from the INSTRON 3382 frame-mounted probe. The specimen dimensions were 56 × 10 × 1 mm and the workspace size was 32 × 6 × 1 mm.

The fractography study was carried out on a TM4000 (Hitachi, Tokyo, Japan) scanning electron microscope. For study in raster mode, the samples were glued on a copper substrate using conductive carbon glue, and the accelerating voltage was 15 kV.

3. Results

3.1. Light Microscopy of Microstructures of Ti-(36-40)Zr-9Nb Alloys

Images of the microstructure after melting, rolling, and rolling and quenching are shown in Figure 1, Figure 2, and Figure 3, respectively.

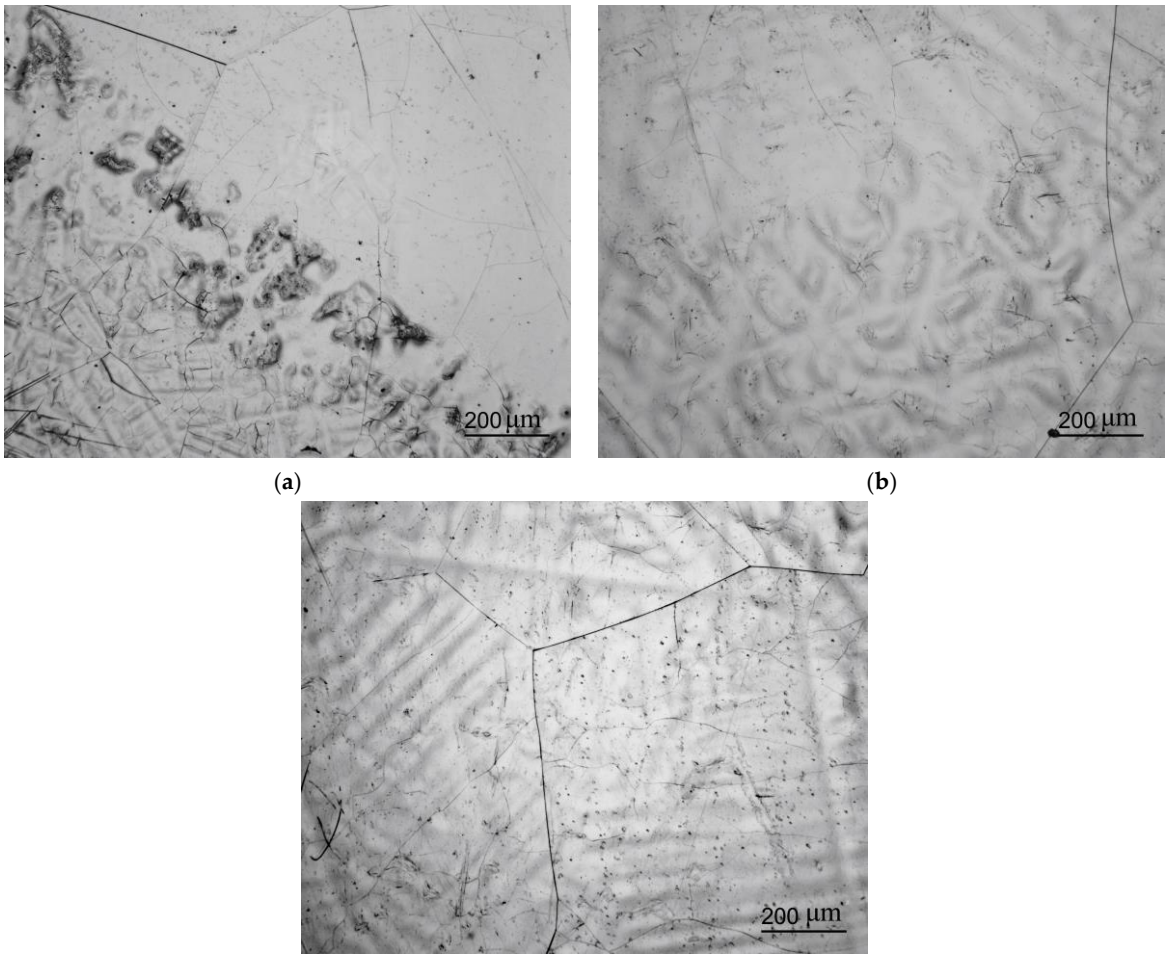

(**a**) (**b**)

(**c**)

Figure 1. Microstructure of the ingots after melting: (**a**)—Ti-36Zr-9Nb; (**b**)—Ti-38Zr-9Nb; (**c**)—Ti-40Zr-9Nb.

After melting, the microstructure of ingots has a pronounced dendritic structure. This structure is typical of titanium alloys containing refractory elements that have not undergone additional heat treatment and is due to earlier crystallization of niobium and zirconium in relation to titanium at a rather slow cooling rate, which cannot be increased in the furnace used.

The microstructure of the plates in the longitudinal and cross-section of the plates is homogeneous after both rolling and quenching and consists of β grains of polyhedral shape. After rolling, the grain size in diameter is in the range of 30 and 100 µm, and the uniformity of the grains can be explained by the preheating of the billets and contact with the massive cold rolls of the rolling mill. The grain size after quenching is in the range of 50 and 170 µm. Grain growth is associated with the onset of recrystallization.

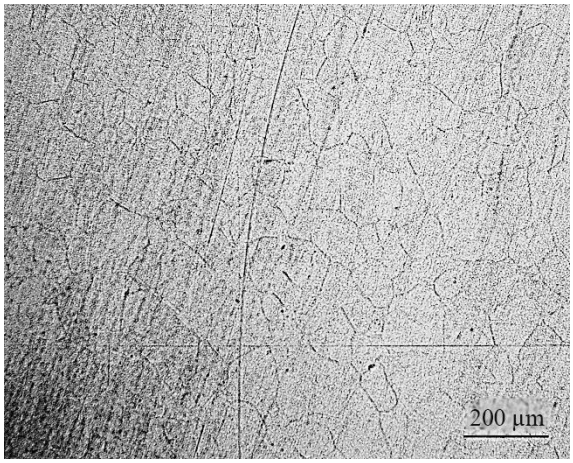

(**a**)

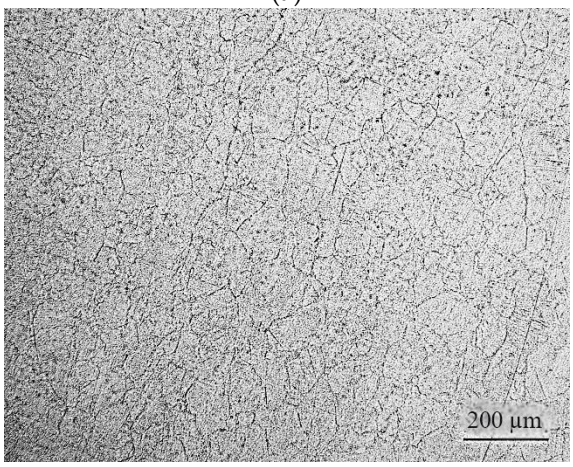

(**b**)

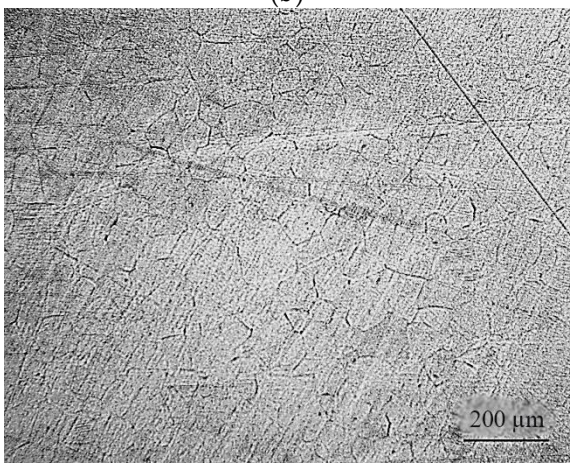

(**c**)

Figure 2. Microstructure of the plates after rolling: (**a**)—Ti-36Zr-9Nb; (**b**)—Ti-38Zr-9Nb; (**c**)—Ti-40Zr-9Nb.

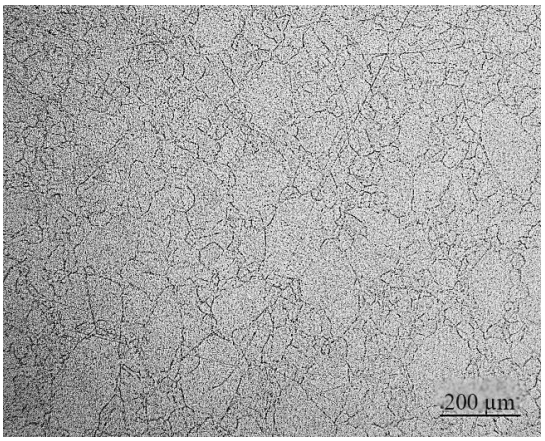

(**a**)

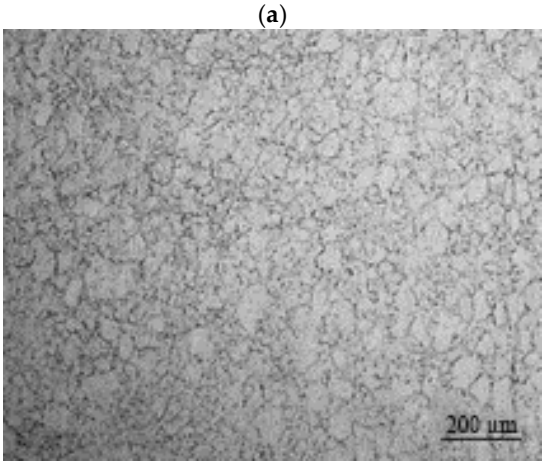

(**b**)

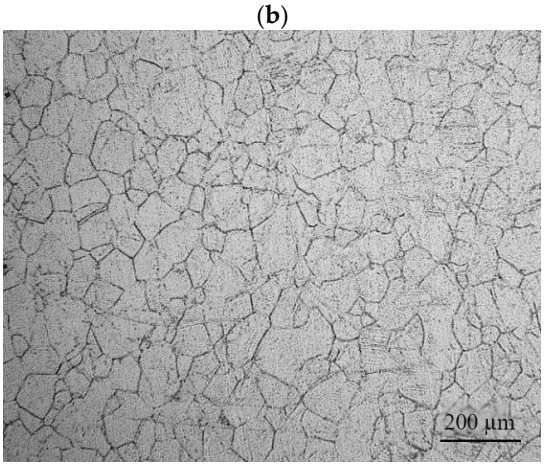

(**c**)

Figure 3. Microstructure of the plates after rolling and quenching: (**a**)—Ti-36Zr-9Nb; (**b**)—Ti-38Zr-9Nb; (**c**)—Ti-40Zr-9Nb.

3.2. X-ray Phase Analysis (XRF) of Ti-(36-40)Zr-9Nb Alloys

The results of X-ray phase analysis of the composition of plates after rolling and after rolling and quenching are presented in Table 3 and Figure 4. The alloys after rolling consist only of metastable β-Ti. This is due to the influence of β-stabilizer Nb and neutral element Zr [42]. On its own, zirconium is a neutral hardener, but in the presence of other β-stabilizers, it also weakly stabilizes the β-phase. The phase composition of ingots does not change after quenching. This is because the β-phase formed during heating before rolling is fixed. After rolling and quenching, the alloys also consist of only β-phase. Quenching stabilizes the metastable high-temperature phase, promoting a uniform composition.

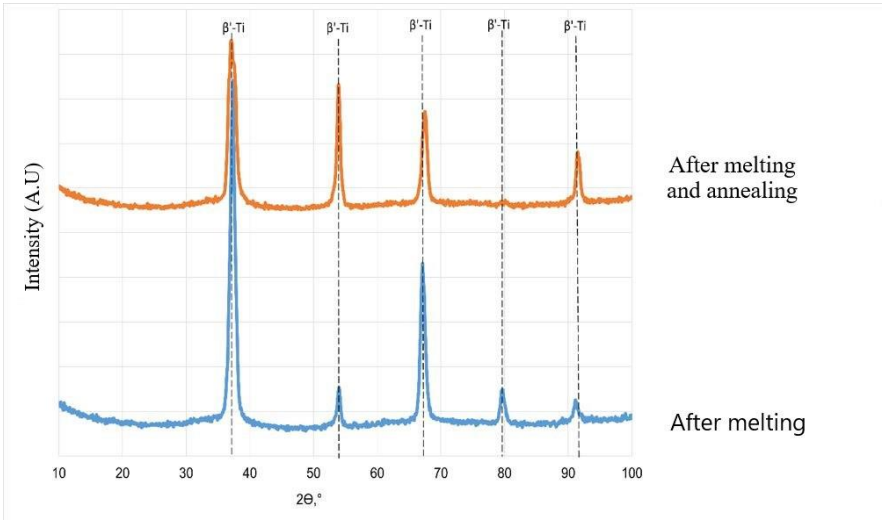

(**a**)

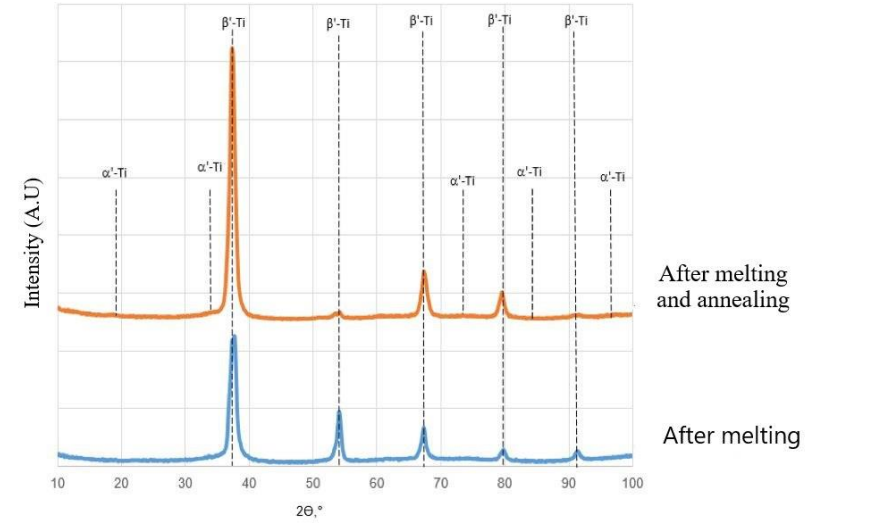

(**b**)

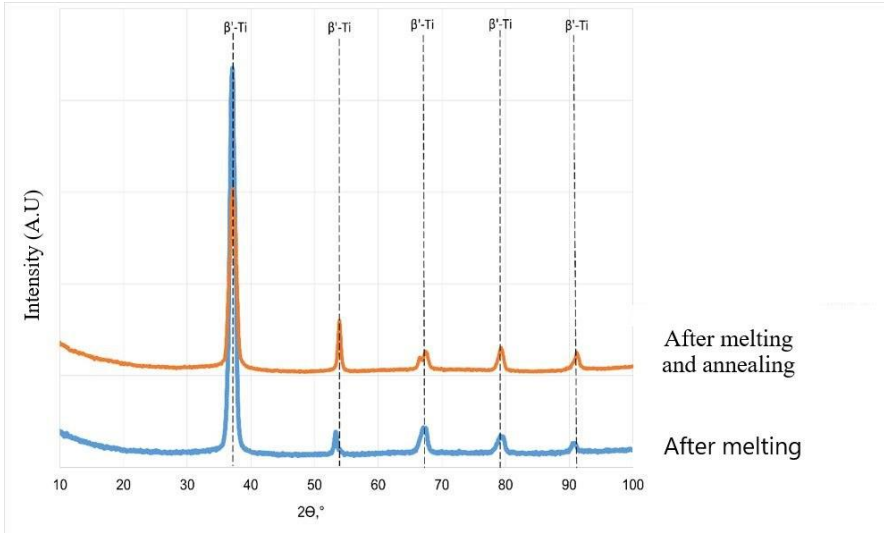

(**c**)

Figure 4. X-ray diffraction patterns of alloys: (**a**)—Ti-36Zr-9Nb; (**b**)—Ti-38Zr-9Nb; (**c**)—Ti-40Zr-9Nb.

Table 3. Phase composition of Ti-(36-40)Zr-9Nb alloy plates before and after quenching.

Composition	Condition	Phase Structure	Type of Crystal Lattice	Contents, Volume. %	Crystal Lattice Parameters
Ti-36Zr-9Nb	After the rolling process	β-Ti	type A2, cI2	100	a = 3.40141 ± 0.00006 Å
	After the rolling process and quenching	β-Ti	type A2, cI2	100	a = 3.40210 ± 0.00002 Å
Ti-38Zr-9Nb	After the rolling process	β-Ti	type A2, cI2	100	a = 3.40842 ± 0.00005 Å
	After the rolling process and quenching	β-Ti	type A2, cI2	100	a = 3.40913 ± 0.00004 Å
Ti-40Zr-9Nb	After the rolling process	β-Ti	type A2, cI2	100	a = 3.42241 Å
	After the rolling process and quenching	β-Ti	type A2, cI2	100	a = 3.41362 ± 0.00004 Å

3.3. Microhardness of Ti-(36-40)Zr-9Nb Alloys

The results of plate microhardness analysis after rolling and quenching are presented in Table 4.

Table 4. Microhardness of Ti-(36-40)Zr-9Nb plates.

Composition	Condition	Microhardness, HV
Ti-36Zr-9Nb	After the rolling process	223 ± 2
	After the rolling process and quenching	219 ± 1
Ti-38Zr-9Nb	After the rolling process	216 ± 2
	After the rolling process and quenching	216 ± 2
Ti-40Zr-9Nb	After the rolling process	219 ± 2
	After the rolling process and quenching	213 ± 2

Microhardness of plates after quenching insignificantly decreases for all studied compositions. Quenching does not change the phase composition and very insignificant decrease in hardness is associated only with some increase in grain size due to partial recrystallization. In the plate Ti-38Zr-9Nb microhardness after quenching practically did not change, due to the small heating time for the beginning of recrystallization.

3.4. Mechanical Properties

The results of mechanical tests of Ti-(36-40)Zr-9Nb alloy are presented in Table 5. Typical tensile diagrams are shown in Figures 5–7.

Table 5. Mechanical properties of Ti-36Zr-9Nb plates.

State	δ, %	$\sigma_{0.2}$, MPa	σ_B, MPa
	Ti-36Zr-9Nb		
After the rolling process	11.8 ± 1.9	484 ± 69	637 ± 21
After the rolling process and quenching	19.3 ± 2.0	289 ± 20	628 ± 20
	Ti-38Zr-9Nb		
After the rolling process	14.4 ± 2.1	494 ± 35	656 ± 6
After the rolling process and quenching	23.0 ± 1.8	324 ± 17	613 ± 15
	Ti-40Zr-9Nb		
After the rolling process	8.9 ± 1.0	532 ± 23	604 ± 15
After the rolling process and quenching	23.4 ± 0.5	364 ± 25	594 ± 29

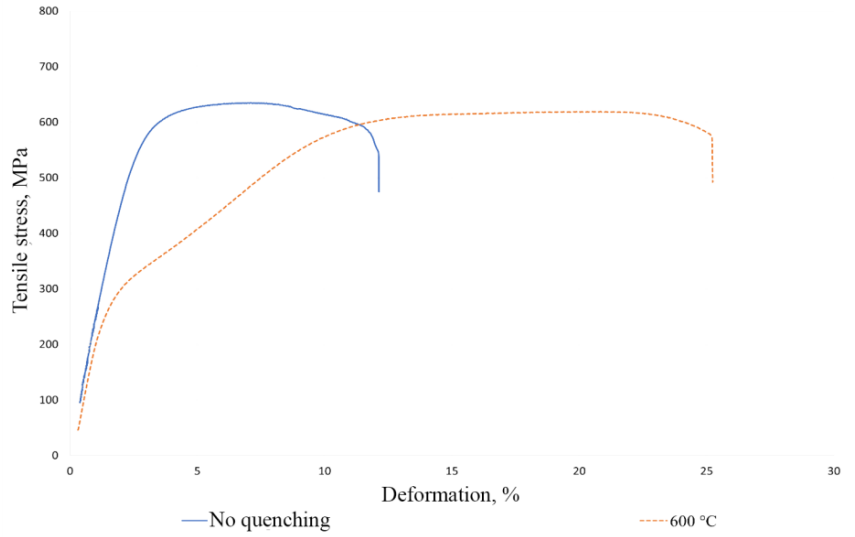

Figure 5. Tensile diagram of Ti-36Zr-9Nb alloy samples.

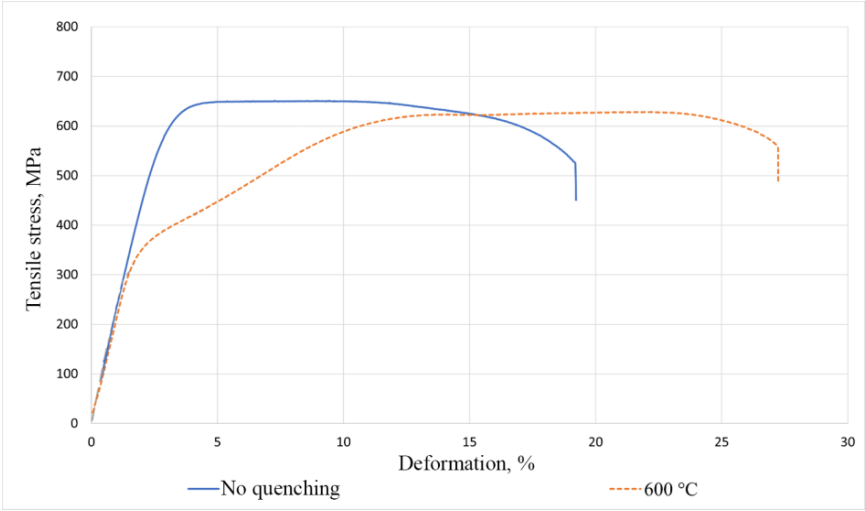

Figure 6. Tensile diagram of Ti-38Zr-9Nb alloy samples.

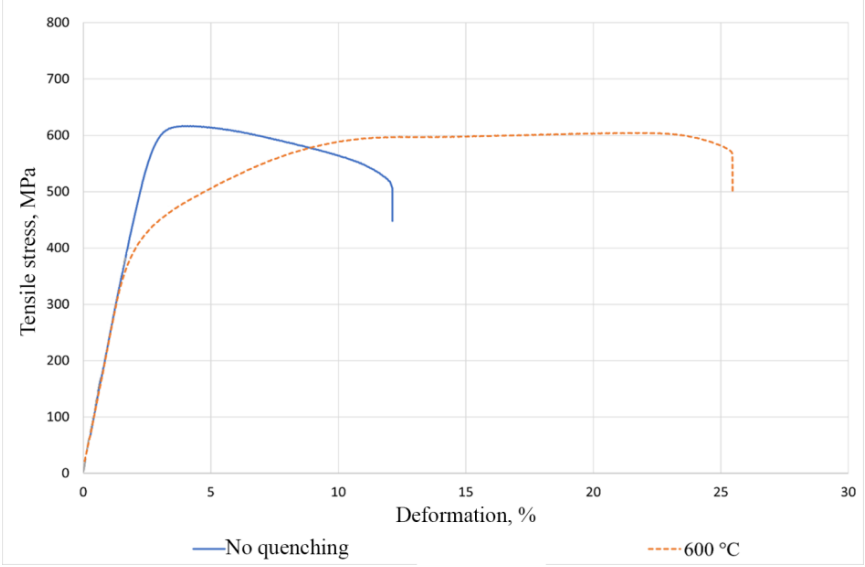

Figure 7. Tensile diagram of Ti-40Zr-9Nb alloy samples.

Based on the diagrams and the values obtained, it is noted that after rolling hardening led to an increase in the ductility of all studied alloys Ti-(36-40)Zr-9Nb with an approximate preservation of the strength level. The alloy Ti-38Zr-9Nb showed the highest strength.

The linearly increasing section on each diagram demonstrates elastic deformation proceeding according to Hooke's law. After it, a kinked area appears in the hardened samples, indicating the yield strength associated with reversible phase change: β'<-> α". The β'-phase has a crystal lattice like the β-phase, and the presence of a kink in the mechanical studies' images can distinguish the state of the material in which the metastable β-phase is present. The α"-phase is an intermediate phase of the β → α'-transformation and is the result of an incomplete shift and requires much smaller atomic displacements than the formation of the α- and α'-phase [43]. The phase transition is realized by a shear mechanism. The cause of the phase transition is loading and the plastic deformation that takes place. The occurring phase change means the manifestation of hysteresis behavior in the compositions. Following this site, a region is observed in which the load is practically unchanged and the specimen undergoes tensile strain.

3.5. Cyclical Loading

Figures 8–10 show the tensile diagrams for cyclic loading up to 8% strain for 10 cycles.

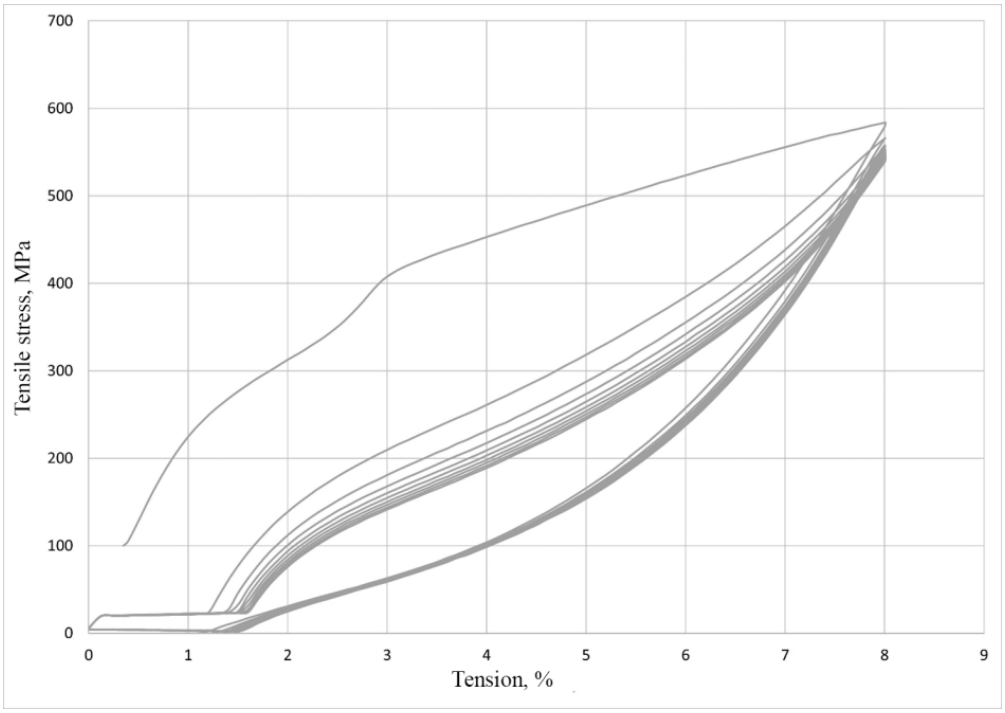

Figure 8. Cyclic loading of the alloy Ti-36Zr-9Nb.

Three compositions were studied at cyclic strain up to 8%, and the lowest residual strain was shown by alloy 38%; therefore, additional studies were made on this alloy at cyclic strains of 2, 3, and 6%. It was of interesting to observe at what maximum strain the residual strain would be as close to 0 as possible. For Ti-38Zr-9Nb, the samples were cyclically stretched to 2%, 3%, 6%, and 8% (Figure 11).

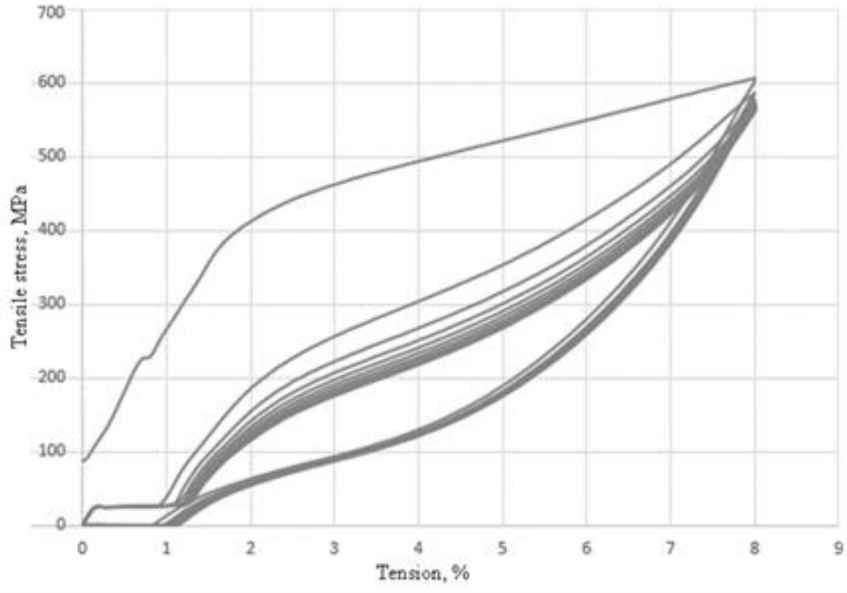

Figure 9. Cyclic loading of the alloy Ti-36Zr-9Nb.

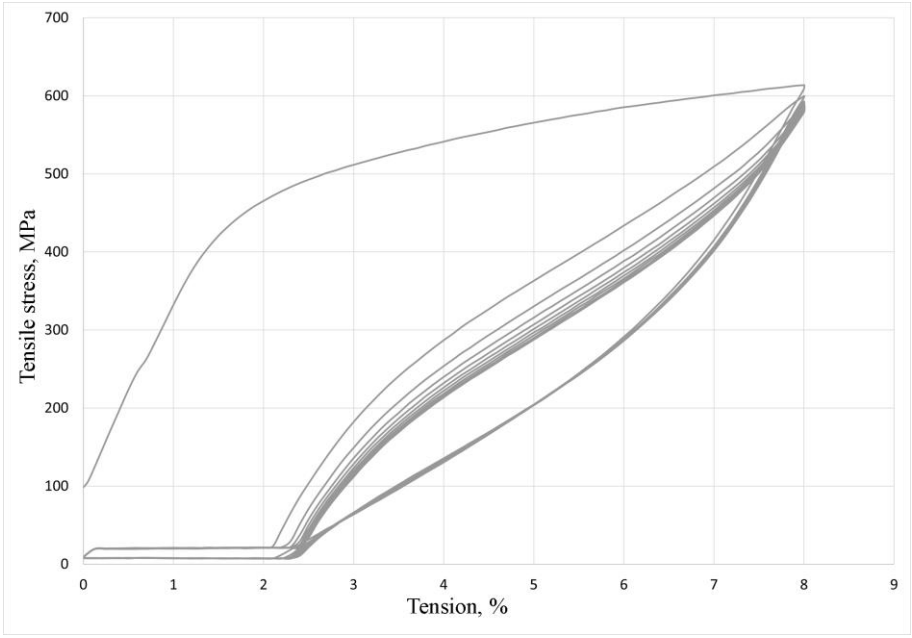

Figure 10. Cyclic loading of the alloy Ti-40Zr-9Nb.

Ti-36Zr-9Nb exhibited a residual strain equal to 1.5%.

Ti-38Zr-9Nb returns with the lowest residual strain when loaded to 2% and 3%. At 6%, the residual strain is 0.4%, and at a loading of 8% = 0.7%.

Ti-40Zr-9Nb exhibits a residual strain equal to 2.4%, which is the worst result.

The linear plot in each diagram demonstrates the transition of metastable β-phase to α''. In this regard, it can be concluded that the best hysteresis behavior, which characterizes the manifestation of the superelasticity effect, shows the Ti-38Zr-9Nb alloy.

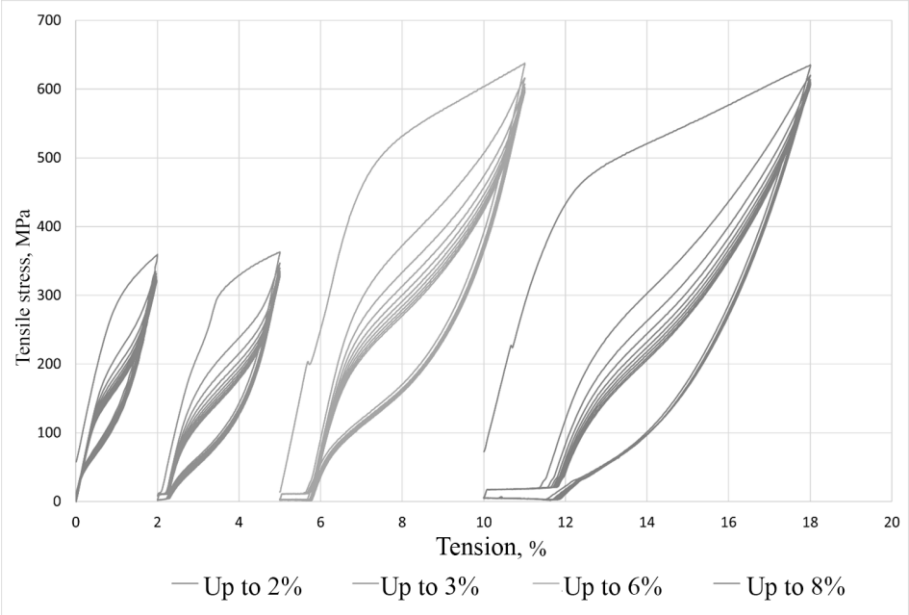

Figure 11. Cyclic loading of the alloy Ti-38Zr-9Nb.

3.6. Young's Modulus

The results of the study of the elastic modulus of plates after rolling and quenching are presented in Table 6.

Table 6. Young's modulus values of plates.

Composition	E, GPa
Ti-36Zr-9Nb	55 ± 2
Ti-38Zr-9Nb	59 ± 3
Ti-40Zr-9Nb	51 ± 2

In general, the E values of all alloys were approximately the same and are already quite close to the E value for human bone tissue. According to the test results, the alloy Ti-40Zr-9Nb, compared to the others, had slightly lower E values, which is due to the largest amount of Zr, which weakens the bond between atoms in the presence of β-stabilizer.

3.7. Fractography

Figure 12 shows a typical view of the fracture surface under static loading for samples of Ti-40Zr-9Nb alloy after rolling and quenching: 1—crack nucleation surface; 2—ductile fracture surface; 3—brittle fracture surface before fracture. Fracture direction from surface 1 to the center of the specimen.

In the fracture zones, there are both brittle fracture areas in the form of "jet patterns" and ductile areas in the form of "pits". When the specimens are hardened, the brittle fracture areas decrease; more ductile fracture areas appear; the crystallographic character of the fracture takes the form of shearing or bilateral shearing to the center of the specimen; the appearance of fractures becomes more fibrous or ductile, which corresponds to the results of mechanical tests; and the formation of a neck is observed. In all specimens, the crack leading to failure occurred on the surface and propagated through the center to the opposite outside of the specimens, or from two opposite surfaces to the center.

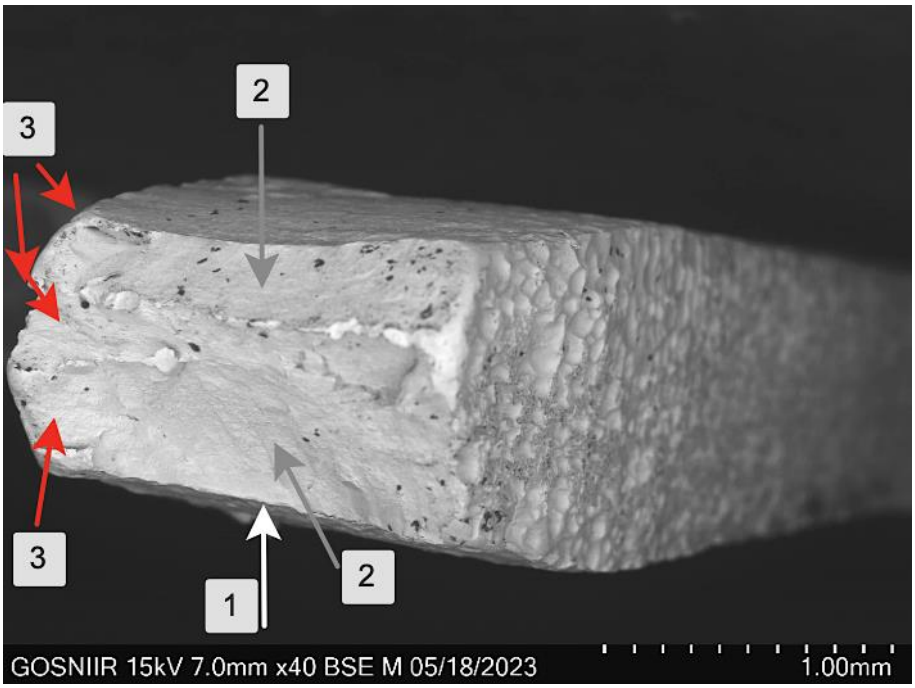

(**a**)

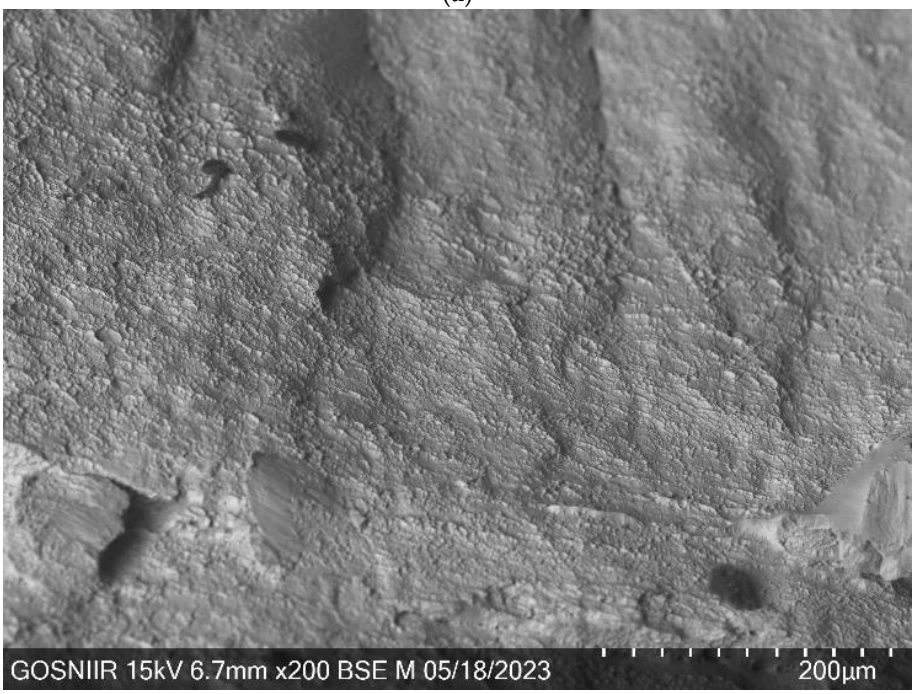

(**b**)

Figure 12. Fractography of Ti-40Zr-9Nb alloy after rolling and quenching: (**a**) general view of static fracture; (**b**) view of fracture surface.

4. Conclusions

It was found that alloys (at. %) Ti-36Zr-9Nb, Ti-38Zr-9Nb, and Ti-40Zr-9Nb both after rolling and after rolling and quenching have a homogeneous microstructure consisting of polyhedral grains of β-Ti stabilized by Nb and Zr. The grain size after rolling is ~100 μm and after quenching is ~170 μm.

Quenching is rational for the studied alloys, as it has practically no effect on Young's modulus E, microhardness, or strength characteristics, but increases plasticity and the

manifestation of the superelasticity effect. The achieved values of E ~ 50–60 GPa are quite close to the E values in human bone tissues.

Alloy Ti-38Zr-9Nb has the most balanced complex of mechanical characteristics in comparison with the other two alloys: at approximately the same values of E and microhardness, it has greater strength and plasticity characteristics, and it has a more pronounced effect of superelasticity.

In connection with the rather high mechanical properties (ultimate strength σv ~ 630–660 MPa, plasticity δ ~ 14–23%) of the studied alloys and more optimal modulus of elasticity in relation to pure titanium and titanium Grade 5, it seems appropriate to further study the material for biological compatibility and corrosion resistance.

Author Contributions: Conceptualization, S.V.K. and L.A.S.; Data curation, M.A.K., E.O.N. and L.A.S.; Formal analysis, K.V.S. and S.V.K.; Funding acquisition, M.A.S. (Mikhail A. Sevostyanov) and A.G.K.; Investigation, K.V.S., S.V.K., M.A.K., Y.G., M.A.S. (Maria A. Sudarchikova), T.M.S. and S.A.M.; Methodology, S.V.K., A.D.G., M.A.S. (Maria A. Sudarchikova), T.M.S. and S.A.M.; Project administration, M.A.S. (Mikhail A. Sevostyanov) and A.G.K.; Resources, E.O.N. and A.G.K.; Supervision, A.D.G. and A.G.K.; Validation, A.D.G. and Y.A.M.; Visualization, Y.G. and Y.A.M.; Writing—original draft, K.V.S. and Y.G.; Writing—review and editing, M.A.K. and M.A.S. (Maria A. Sudarchikova) All authors have read and agreed to the published version of the manuscript.

Funding: This work was supported by the grant of the Russian Science Foundation No. 24-13-00186, https://rscf.ru/project/24-13-00186/.

Institutional Review Board Statement: Not applicable.

Data Availability Statement: The original contributions presented in this study are included in the article. Further inquiries can be directed to the corresponding author(s).

Conflicts of Interest: The authors declare no conflicts of interest. The funders had no role in the design of the study; in the collection, analyses, or interpretation of data; in the writing of the manuscript; or in the decision to publish the results. All the authors have reviewed the manuscript and agree on submission to your journal.

References

1. Pagani, S.; Liverani, E.; Giavaresi, G.; De Luca, A.; Belvedere, C.; Fortunato, A.; Leardini, A.; Fini, M.; Tomesani, L.; Caravaggi, P. Mechanical and in vitro biological properties of uniform and graded Cobalt-chrome lattice structures in orthopedic implants. *J. Biomed. Mater. Res. B Appl. Biomater.* **2021**, *109*, 2091–2103. [CrossRef] [PubMed]
2. Semlitsch, M. Mechanical Properties of Selected Implant Metals Used for Artificial Hip Joints. In *Metal and Ceramic Biomaterials*; CRC Press: Boca Raton, FL, USA, 2018; pp. 1–22. [CrossRef]
3. Aherwar, A.; Singh, A.; Patnaik, A. Cobalt Based Alloy: A Better Choice Biomaterial for Hip Implants. *Trends Biomater. Artif. Organs* **2016**, *30*, 50–55.
4. Kilner, T.; Laanemäe, W.M.; Pilliar, R.; Weatherly, G.C.; MacEwen, S.R. Static mechanical properties of cast and sinter-annealed cobalt-chromium surgical implants. *J. Mater. Sci.* **1986**, *21*, 1349–1356. [CrossRef]
5. Dewidar, M.M.; Yoon, H.C.; Lim, J.K. *Mechanical Properties of Metals for Biomedical Applications Using Powder Metallurgy Process: A Review*; Springer: Berlin/Heidelberg, Germany, 2006; Volume 12, pp. 193–206.
6. *ASTM F 75: 2007*; Standard Specification for Cobalt-28 Chromium-6 Molybdenum Alloy Castings and Casting Alloy for Surgical Implants (UNS R30075). American Society for Testing and Materials: West Conshohocken, PA, USA, 2007.
7. Hoffmeister, B.K.; Smith, S.R.; Handley, S.M.; Rho, J.Y. Anisotropy of Young's modulus of human tibial cortical bone. *Med. Biol. Eng. Comput.* **2000**, *38*, 333–338. [CrossRef]
8. Keller, T.S.; Mao, Z.; Spengler, D.M. Young's modulus, bending strength, and tissue physical properties of human compact bone. *J. Orthop. Res.* **1990**, *8*, 592–603. [CrossRef]
9. Raffa, M.L.; Nguyen, V.-H.; Hernigou, P.; Flouzat-Lachaniette, C.-H.; Haiat, G.; Traumatologique, H.; Mondor, A.-H.; Paris, C. Stress shielding at the bone-implant interface: Influence of surface roughness and of the bone-implant. *J. Orthop. Res.* **2021**, *39*, 1174–1183. [CrossRef]
10. Noyama, Y.; Miura, T.; Ishimoto, T.; Itaya, T.; Niinomi, M.; Nakano, T. Bone loss and reduced bone quality of the human femur after total hip arthroplasty under stress-shielding effects by titanium-based implant. *Mater. Trans.* **2012**, *53*, 565–570. [CrossRef]
11. Shahzamanian, M.; Banerjee, R.; Dahotre, N.B.; Srinivasa, A.R.; Reddy, J. Analysis of stress shielding reduction in bone fracture fixation implant using functionally graded materials. *Compos. Struct.* **2023**, *321*, 117262. [CrossRef]
12. Zhang, Q.; Cossey, A.; Tong, J. Stress shielding in periprosthetic bone following a total knee replacement: Effects of implant. *Med Eng. Phys.* **2016**, *38*, 1481–1488. [CrossRef]

13. Capón-García, D.; López-Pardo, A.; Alves-Pérez, M.T. Causes for revision surgery in total hip replacement. A retrospective epidemiological analysis. *Rev. Española Cirugía Ortopédica Traumatol. Engl. Ed.* **2016**, *60*, 160–166. [CrossRef]
14. Bjorklund, G.; Stejskal, V.; Urbina, M.A.; Dadar, M.; Chirumbolo, S.; Mutter, J. Metals and Parkinson's Disease: Mechanisms and Biochemical Processes. *Curr. Med. Chem.* **2018**, *25*, 2198–2214. [CrossRef] [PubMed]
15. Yokel, R. The Toxicology of Aluminum in the Brain: A Review. *NeuroToxicology* **2000**, *21*, 813–828. [PubMed]
16. Guo, C.H.; Lu, Y.F.; Hsu, G.S.W. The influence of aluminum exposure on male reproduction and offspring in mice. *Environ. Toxicol. Pharmacol.* **2005**, *20*, 135–141. [CrossRef] [PubMed]
17. Tripathi, D.; Mani, V.; Pal, R.P. Vanadium in Biosphere and Its Role in Biological Processes. *Biol. Trace Elem. Res.* **2018**, *186*, 52–67. [CrossRef]
18. Assem, F.L.; Oskarsson, A. Vanadium. In *Handbook on the Toxicology of Metals*; Elsevier: Amsterdam, The Netherlands, 2015; pp. 1347–1367. [CrossRef]
19. Wilk, A.; Szypulska-Koziarska, D.; Wiszniewska, B. The toxicity of vanadium on gastrointestinal, urinary and reproductive system, and its influence on fertility and fetuses malformations. *Postep. Hig. I Med. Dosw.* **2017**, *71*, 850–859. [CrossRef]
20. Leite, K.L.F.; Dias, M.O.; Tavares, F.O.M.; Silva, K.S.; Chevitarese, A.B.; Martins, M.L.; Masterson, D.; de Menezes, L.R.; Gonçalves, A.F.; Maia, L.C. A Data mining analysis on niobium in dentistry: Promising alloys for dental materials. *Pesqui. Bras. Odontopediatria Clín. Integr.* **2024**, *24*, e230072. [CrossRef]
21. Hsu, H.C.; Wu, S.C.; Fang, W.C.; Ho, W.F. Experimental Investigation of the Impact of Niobium Additions on the Structural Characteristics and Properties of Ti–5Cr–xNb Alloys for Biomedical Applications. *Materials* **2024**, *17*, 1667. [CrossRef]
22. Marković, G.; Manojlović, V.; Ružić, J.; Sokić, M. Predicting Low-Modulus Biocompatible Titanium Alloys Using Machine Learning. *Materials* **2023**, *16*, 6355. [CrossRef]
23. Tang, J.; Yang, H.; Qian, B.; Zheng, Y.; Vermaut, P.; Prima, F.; Sun, F. TWIP-assisted Zr alloys for medical applications: Design strategy, mechanical properties and first biocompatibility assessment. *J. Mater. Sci. Technol.* **2024**, *184*, 32–42. [CrossRef]
24. Chattopadhyay, K.; Mandal, M.; Maiti, D.K. A review on zirconium-based metal–organic frameworks: Synthetic approaches and biomedical applications. *Mater. Adv. R. Soc. Chem.* **2024**, *5*, 51–67. [CrossRef]
25. Abdel-Hady, M.; Hinoshita, K.; Morinaga, M. General approach to phase stability and elastic properties of β-type Ti-alloys using electronic parameters. *Scr. Mater.* **2006**, *55*, 477–480. [CrossRef]
26. Meng, Q.; Zhang, J.; Huo, Y.; Sui, Y.; Zhang, J.; Guo, S.; Zhao, X. Design of low modulus β-type titanium alloys by tuning shear modulus C44. *J. Alloys Compd.* **2018**, *745*, 579–585. [CrossRef]
27. Sergienko, K.V.; Mikhailova, A.V.; Konushkin, S.V.; Kaplan, M.A.; Nasakina, E.O.; Sevost'yanov, M.A.; Baikin, A.S.; Kolmakov, A.G. Effect of Heat Treatment on the Mechanical Properties of Ti–Nb–Mo–Zr–Al Alloys. *Russ. Metall. Met.* **2022**, *2022*, 735–740. [CrossRef]
28. Konushkin, S.V.; Kaplan, M.A.; Sergienko, K.V.; Gorbenko, A.D.; Morozova, Y.A.; Ivannikov, A.Y.; Sudarchikova, M.A.; Sevostyanova, T.M.; Nasakina, E.O.; Mikhlik, S.A.; et al. Effect of Heat Treatment on the Structure and Mechanical Properties of Ti–10Nb–(1–3)Mo Alloys. *Inorg. Mater. Appl. Res.* **2024**, *15*, 395–401. [CrossRef]
29. Volchikhina, M.A.; Konushkin, S.V.; Mikhlik, S.A.; Sergienko, K.V.; Kaplana, M.A.; Gorbenko, A.D.; Sevostyanova, T.M.; Kolmakov, A.G.; Sevostyanov, M.A. The Structure and Mechanical Properties of Ti–(36–40)Zr–9Ta (at %) Alloys for Medical Purposes. *Inorg. Mater. Appl. Res.* **2024**, *15*, 1321–1328. [CrossRef]
30. Hanawa, T. Biocompatibility of titanium from the viewpoint of its surface. *Sci. Technol. Adv. Mater.* **2022**, *23*, 457–472. [CrossRef]
31. Möller, B.; Terheyden, H.; Ail, Y.; Purcz, N.M.; Hertrampf, K.; Tabakov, A.; Behrens, E.; Wiltfang, J. A comparison of biocompatibility and osseointegration of ceramic and titanium implants: An in vivo and in vitro study. *Int. J. Oral Maxillofac. Surg.* **2012**, *41*, 638–645. [CrossRef]
32. Wang, Q.; Dong, C.; Liaw, P.K. Structural Stabilities of β-Ti Alloys Studied Using a New Mo Equivalent Derived from [β/(α + β)] Phase-Boundary Slopes. *Met. Mater. Trans. A* **2015**, *46*, 3440–3447. [CrossRef]
33. Wang, J.; Qi, X.; Xing, X.; Peng, Y.; Huang, G.; Wang, B.L.; Li, L.; Zheng, Y.F. In vitro cytotoxicity and hemocompatibility studies of Ti-Nb, Ti-Nb-Zr and Ti-Nb-Hf biomedical shape memory alloys. *Biomed. Mater.* **2010**, *5*, 044102. [CrossRef]
34. Kim, H.Y.; Fu, J.; Tobe, H.; Kim, J.I.; Miyazaki, S. Crystal Structure, Transformation Strain, and Superelastic Property of Ti–Nb–Zr and Ti–Nb–Ta Alloys. *Shape Mem. Superelasticity* **2015**, *1*, 107–116. [CrossRef]
35. Collings, E.W. *The Physical Metallurgy of Titanium Alloys*; American Society for Metals: Metals Park, OH, USA, 1984.
36. Fellah, M.; Hezil, N.; Bouras, D.; Habeeb, M.A.; Hamadi, F.; Bouchareb, N.; El-Hiti, G.A. Microstructural and photocatalytic properties of nanostructured near-β Ti-Nb-Zr alloy for total hip prosthesis use. *Kuwait J. Sci.* **2024**, *51*, 100276. [CrossRef]
37. Korenev, A.A.; Illarionov, A.G. The Effect of Cold Deformation on the Structure, Texture, Elastic and Microdurometric Properties of Biocompatible Beta-Titanium Alloys Based on Ti–Nb–Zr System. *Phys. Met. Metallogr.* **2023**, *124*, 575–582. [CrossRef]
38. Korenev, A.A.; Illarionov, A.G.; Karabanalov, M.S. Formation of Structural-Phase State and Elastic and Durometric Properties of Biocompatible Cold-Rolled Titanium Ti–Nb–Zr-Based Alloys during Aging. *Phys. Met. Metallogr.* **2024**, *125*, 313–323. [CrossRef]
39. Wang, B.; Chen, Y.; Xu, Z.; Chen, C.; Zhang, J. Deformation induced self-accommodation morphology transition from triangular to nano-twinned martensite in Ti-Nb-Zr shape memory alloys. *Scr. Mater.* **2024**, *245*, 116054. [CrossRef]
40. Karakurt, E.M.; Cetin, Y.; Incesu, A.; Demirtas, H.; Kaya, M.; Yildizhan, Y.; Tosun, M.; Huang, Y. Microstructural, Biomechanical, and In Vitro Studies of Ti-Nb-Zr Alloys Fabricated by Powder Metallurgy. *Materials* **2023**, *16*, 4240. [CrossRef]

41. *NIST SRM-1976a*; Calibration Standard for High-Resolution X-Ray Diffraction. National Institute of Standarts and Technology: Gaithersburg, MD, USA, 2012.
42. Pesode, P.; Barve, S. A review—Metastable β titanium alloy for biomedical applications. *J. Eng. Appl. Sci.* **2023**, *70*, 1–36. [CrossRef]
43. Popov, A.A. *Phase and Structural Transformations in Metal Alloys: Textbook*; Popov, A.A., Zhilyakova, M.A., Zorina, M.A., Eds.; Izd-e Ural. un-ta: Yekaterinburg, Russia, 2018; 316p.

Disclaimer/Publisher's Note: The statements, opinions and data contained in all publications are solely those of the individual author(s) and contributor(s) and not of MDPI and/or the editor(s). MDPI and/or the editor(s) disclaim responsibility for any injury to people or property resulting from any ideas, methods, instructions or products referred to in the content.